

Functional network inference of the suprachiasmatic nucleus

John H. Abel^{a,b,1}, Kirsten Meeker^{c,1}, Daniel Granados-Fuentes^d, Peter C. St. John^{a,e}, Thomas J. Wang^d, Benjamin B. Bales^c, Francis J. Doyle III^{a,f}, Erik D. Herzog^d, and Linda R. Petzold^{c,2}

^aDepartment of Chemical Engineering, University of California, Santa Barbara, CA 93106; ^bSystems Biology Program, Harvard University, Cambridge, MA 02138; ^cDepartment of Computer Science, University of California, Santa Barbara, CA 93106; ^dDepartment of Biology, Washington University in St. Louis, St. Louis, MO 63130; ^eBiosciences Center, National Renewable Energy Laboratory, Golden, CO 80401; and ^fHarvard John A. Paulson School of Engineering and Applied Sciences, Harvard University, Cambridge, MA 02138

Edited by Joseph S. Takahashi, Howard Hughes Medical Institute, University of Texas Southwestern Medical Center, Dallas, TX, and approved March 7, 2016 (received for review November 3, 2015)

In the mammalian suprachiasmatic nucleus (SCN), noisy cellular oscillators communicate within a neuronal network to generate precise system-wide circadian rhythms. Although the intracellular genetic oscillator and intercellular biochemical coupling mechanisms have been examined previously, the network topology driving synchronization of the SCN has not been elucidated. This network has been particularly challenging to probe, due to its oscillatory components and slow coupling timescale. In this work, we investigated the SCN network at a single-cell resolution through a chemically induced desynchronization. We then inferred functional connections in the SCN by applying the maximal information coefficient statistic to bioluminescence reporter data from individual neurons while they resynchronized their circadian cycling. Our results demonstrate that the functional network of circadian cells associated with resynchronization has small-world characteristics, with a node degree distribution that is exponential. We show that hubs of this small-world network are preferentially located in the central SCN, with sparsely connected shells surrounding these cores. Finally, we used two computational models of circadian neurons to validate our predictions of network structure.

systems biology | synchronization | circadian oscillator | biological clock | mathematical model

Circadian rhythms are endogenous oscillations in behavior and gene expression with near-24-h periodicity observed in most living organisms. Circadian rhythms are known to regulate a wide range of processes including cell cycles, body temperature, metabolism, and behavior (1–5). The mammalian suprachiasmatic nucleus (SCN), a network of ~20,000 neurons located in the hypothalamus of the brain, functions as the body's master pacemaker and mediates the entrainment of peripheral tissue oscillators to light/dark cycles (6, 7). Although individual neurons within the SCN act as autonomous circadian pacemakers, they display stochastic variation in period length and must communicate to maintain stable period lengths and phase relationships for system-wide control of daily cycles (8–10). SCN network dynamics are contingent on properties of the cell-autonomous oscillator (11, 12), communication via neurotransmitters (10, 13–16), and the underlying connectivity of the network.

Neurons in the SCN generate circadian oscillations through a transcription-translation feedback loop and are known to synchronize by the timely release of vasoactive intestinal peptide (VIP) and GABA neurotransmitters, which modulate the oscillator through the transcription factor CREB (10, 16–19). Although the single-cell oscillator and coupling pathways have been extensively researched, relatively little is known about the structure of the neuronal network driving synchronization in the SCN. Prominent modeling studies of the past decade have assumed a wide variety of network structures: nearest neighbor (15, 20), small-world (21), or mean-field (22, 23), or combinations of these depending on coupling pathway (16), pointing to the high degree of uncertainty regarding the general connectivity of the

SCN. There has been significant recent interest in attempting to elucidate the network structure and mechanisms driving synchrony in the SCN, commonly through light-driven desynchronization assays (19, 24–26). These methods have the advantage of reducing the SCN into large phase clusters of neurons, whose behavior can be easily tracked and modeled with reduced approaches (26). This approach has had great successes in reconciling the roles of GABA and VIP (17, 16, 19, 26). A significant obstacle in developing a mechanistic understanding of synchronization in the SCN is the lack of single-cell resolution in these studies, preventing observation of the dynamics within these clusters. Furthermore, light is received primarily by the core SCN, and this asymmetry of input is entangled with observed SCN behaviors (17). Thus far, only fast-scale (phasic) GABA connections have been mapped at a single-cell resolution (27), and this phasic GABA release is not thought to affect the core oscillator (16).

Here, we present a novel method for inferring the functional network of the suprachiasmatic nucleus during resynchronization at a single-cell resolution. Our strategy involved the application of TTX to disperse single-cell phases through inhibition of intercellular coupling while allowing continued cell-autonomous oscillation (28, 29). TTX was then washed out, restoring coupling and allowing reorganization of the SCN over the following 8 d. We applied the maximal information coefficient (MIC) statistic (30) to bioluminescence recordings during resynchronization to identify “functional connections” within the SCN at a single-cell resolution. Functional connections were defined between neurons that share a high degree of mutual information during

Significance

In mammals, circadian rhythms are controlled by a network of neurons in the brain. The structure of this network dictates organism-wide behavior and adaptation to the environment. We used a neurotoxin to desynchronize this circadian network and then used tools from information theory to determine which cells communicate to establish synchronization. Our results show that this functional network consists of two densely-connected cores, surrounded by sparsely connected shell regions. These findings represent the first time, to our knowledge, that this network has been examined at single cell resolution and show that the importance of these core network regions is independent of light input.

Author contributions: J.H.A., K.M., D.G.-F., P.C.S.J., T.J.W., F.J.D., E.D.H., and L.R.P. designed research; J.H.A., K.M., D.G.-F., P.C.S.J., T.J.W., B.B.B., and E.D.H. performed research; J.H.A., K.M., D.G.-F., P.C.S.J., B.B.B., F.J.D., E.D.H., and L.R.P. analyzed data; and J.H.A., B.B.B., and E.D.H. wrote the paper.

The authors declare no conflict of interest.

This article is a PNAS Direct Submission.

¹J.H.A. and K.M. contributed equally to this work.

²To whom correspondence should be addressed. Email: petzold@engineering.ucsb.edu.

This article contains supporting information online at www.pnas.org/lookup/suppl/doi:10.1073/pnas.1521178113/-DCSupplemental.

resynchronization, characterized by a high MIC score. Although functional connections connote neither causation nor direct physiological connection (31), communication is necessary for SCN neurons to synchronize and maintain precise periodicity (32), resulting in a high mutual information between connected neurons. We used this method to infer networks within five mouse SCN explants. Results showed that the suprachiasmatic nucleus has a consistent resynchronization network with a small-world topology and an exponential node degree distribution in each sample. The most densely connected neurons, or “hubs,” of each network were located in the central SCN. Unlike prior studies involving phase clusters, a second cluster of connected shell neurons was not found. Finally, we related our observed functional networks to the underlying physical network via stochastic simulation using two models of the coupled SCN (33–35).

Results

Design of Resynchronization Experiment. To infer the SCN network, we observed five whole SCN mouse explants resynchronizing after decoupling by TTX (Fig. 1). PERIOD2::Luciferase (PER2::LUC) knock-in SCN explants were cultured while under a microscope, allowing the capture of single-cell bioluminescence within the whole SCN. Bioluminescence counts were recorded each hour, and individual neurons were identified and tracked manually from the resulting images. These single-cell traces are shown in Fig. 1A for SCN1. TTX was applied to the whole tissue explants for 6 d to inhibit intercellular coupling while leaving physical connections within the tissue intact (28, 36, 37). After 6 d, the TTX was washed out, and recordings continued for an additional 8 d as neurons in the network regained synchrony. In the synchronized SCN there was a strong correlation from cycle to cycle for single-cell relative peak times (28). We demonstrate the loss of this hierarchy during TTX application and its restoration after TTX washout in Fig. 1B. Pearson’s r is shown for correlations between peak 0 pre-TTX, and peaks 1–4 at different experimental stages. By day 5 of TTX

application (peak 2), all correlation with peak 0 was effectively removed. Shortly after TTX washout, some correlation was restored, and correlation was completely restored by peak 4 (day 7 post-TTX). In Fig. 1C, correlation with peak 0 for each day is shown. The restoration of correlation in peak times between pre- and post-TTX regions indicated that the original pre-TTX hierarchy was slowly restored over the course of several days post-TTX. Pearson’s r returned to a maximum of ~ 0.7 due to imperfect cell tracking between pre-, during-, and post-TTX conditions. Approximately 40% of cells in each SCN explant lost observable rhythmicity during TTX application, corresponding with ref. 36. These cells were not included in this figure, although they were included in the bioluminescence traces from the post-TTX resynchronization period used to infer network connectivity. A summary of rhythmicity, period distribution, and noise is included as Fig. S1. This protocol resulted in ensembles of single-cell resynchronization traces from five biologically distinct SCNs each containing ~ 400 cells. This dataset is publicly available online at <https://github.com/JohnAbel/scn-resynchronization-data-2016>.

Inferring Connections Between SCN Neurons. Although fast-scale and electrical connections between individual neurons have been identified by methods such as mutual information, transfer entropy, directed transfer functions, Granger causality, or between-sample analysis of connectivity (BSAC) (27, 38–41), these methods are not suitable here due to nonstationary gene expression and the slow-scale nature of VIP and GABA feedback to the core oscillator, resulting in the damping of high-frequency signals (16, 41, 42). High-frequency GABA signals affect the firing of SCN neurons and have been mapped previously (27); however, fast scale GABA is not thought to affect the core oscillator (16). Additionally, due to the limitations of the PER2::LUC bioluminescent reporter used to observe core clock gene expression, the most rapid sampling provides 30-min sample intervals (19), insufficient for methods such as Granger causality (41).

We inferred connections within these samples using the MIC as our correlation metric (30). MIC is effectively a continuous metric of mutual information, and is calculated by partitioning a scatter plot of two variables (in this case, raw bioluminescence recordings of two cells) in phase space into a grid that maximizes the mutual information. We selected this statistic because it readily captures relationships between noisy continuous random variables. MIC scores are high between cells which have identical periods and precise phase relationships, which is indicative of communication to resist the stochastic phase drift that occurs in uncoupled neurons. Strongly or directly connected cells will drift apart less in phase and have more precise periodicity than cells which are unconnected. This point, and the effects of sampling rate, cell amplitudes, and noise on MIC scores are examined via stochastic simulation in Figs. S2 and S3. Because MIC partitions each pair of variables onto a grid and computes the density of grid regions, it effectively performs a normalization of oscillation amplitude: scaling the amplitude of one or both cells will not affect the pairwise MIC score. Notably, MIC shows a bias toward oscillatory states with a small phase offset. To account for this, we repeated the entirety of the following analyses with a phase correction for each cell pair, and show that our results are consistent (Fig. S4).

We applied this correlation metric to pairs of bioluminescence traces from cells from all five SCNs. No detrending or other preprocessing was performed on this data. MIC was calculated using raw bioluminescence of each pair of cells. We then used a receiver operating characteristic (ROC) curve to determine whether the method can differentiate between biologically distinct SCNs and to establish a MIC connectivity threshold that rejects known false positives (Fig. 2). SCN mean phases were aligned before computing MIC for this negative control to prevent biases due to misaligned phase. These five SCNs were cultured separately and bear no common influences; thus, no connections should be found between them. A “possible positive” was defined to be an inferred connection within the same SCN (Fig. 2A), whereas a false positive was a biologically

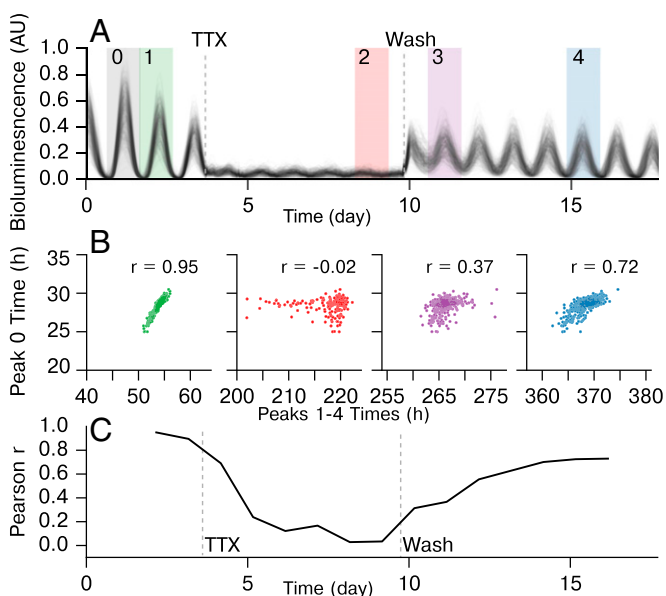


Fig. 1. Experimental protocol demonstrating TTX-mediated resynchronization for SCN1. (A) Bioluminescence traces from individual cells within SCN1, showing pre-TTX, during-TTX, and post-TTX single-cell oscillations. (B) In the functioning SCN, peak times are highly correlated from cycle to cycle. We compare relative peak times 1 (pre-TTX), 2 (during-TTX), and 3–4 (post-TTX), to the first peak (0) to show that a resynchronization is indeed taking place and that the SCN network structure reverts to pre-TTX structure slowly after TTX wash. (C) Plot of Pearson r for correlating each peak to peak 0, showing the resynchronization. Pearson r does not completely return to pre-TTX levels due to inability to track cells accurately across TTX conditions.

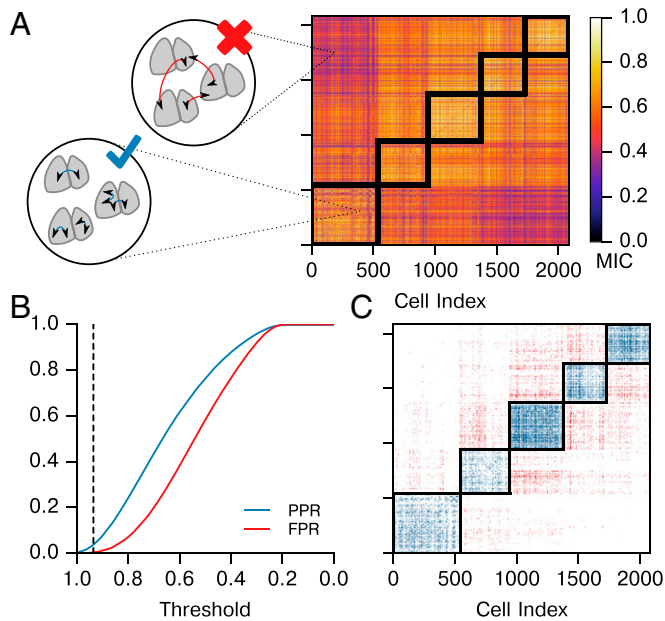


Fig. 2. MIC identifies the strongest connections within a whole SCN sample. (A) Here, we calculate and plot pairwise MIC between neurons from all SCNs. We consider connections within the same SCN to be valid, whether between halves or within a single half. Connections between physiologically distinct SCNs are invalid, as they are biologically infeasible. The block-diagonal regions outlined in black contain valid connections, and connections outside of this region are invalid. (B) False-positive rate (FPR, red, inter-SCN connections) and possible positive rate (PPR, blue, same-SCN connections) are plotted for varying MIC threshold values. We choose an initial threshold of 0.935, for which $FPR = 0.0032$. (C) The connections identified by applying the threshold from B are shown to occur primarily in biologically valid areas (blue), with few invalid connections found (red). Thus, the strongest functional connections within each SCN are identified.

impossible inferred connection between two different SCNs. As it is only known a priori which connections cannot exist, we calculated a possible positive rate (PPR, connections within the same SCN) and false-positive rate (FPR, connections between biologically distinct SCNs) to validate that MIC preferentially detects physiologically valid connectivity.

To infer the network structure within the SCN, we selected a critical MIC parameter, m_{crit} , from this control result. Pairs of cells that have a MIC score above m_{crit} were determined to be functionally connected. Our m_{crit} threshold was chosen to be 0.935, as this value has a 0.0032 FPR while still capturing the strongest connections with $PPR = 0.036$. To account for slight variations in rate of synchronization between SCNs, we adjusted this threshold above m_{crit} for each SCN to normalize average node degree (average number of connections per cell) between networks. Because threshold values were raised, this results in a more conservative estimate of connectivity. For SCNs 1–5, threshold values were raised to 0.949, 0.935, 0.990, 0.968, and 0.969 to yield average node degrees of 4.44, 4.49, 3.94, 4.80, and 4.56, respectively.

SCN Functional Network Displays a Small-World Exponential Architecture.

Networks inferred from the five SCN explants exhibit small-world characteristics as shown in Fig. 3. Small-world networks are commonly found in biological systems and are identified by the average path length L and clustering coefficient C^Δ , as defined in refs. 43 and 44. A network G is determined to be small world if the average path length of G , L_G , is similar to the average path length L_{rand} for the equivalent random graph, and the clustering coefficient C_G^Δ is an order of magnitude greater than C_{rand}^Δ . That is

$$L_G \approx L_{random} \text{ and } C_G^\Delta \gg C_{rand}^\Delta, \quad [1]$$

where the equivalent random graph has the same number of vertices and edges. As shown in Fig. 3, each SCN met the criteria for small-world architecture. Confidence intervals shown for random networks are determined by generation of 10,000 Erdos–Renyi equivalent networks for each SCN. Fig. S5 demonstrates that these network characteristics are consistent across SCNs and locally insensitive to the choice of connectivity threshold.

A semilog plot of the node degree distribution for each SCN is shown as Fig. 4. Similarly to ref. 27, our node degree distribution was best fit with a discrete exponential (geometric) distribution rather than a discrete power law (ζ or Zipf) distribution. The discrete exponential distribution, as defined in ref. 45, is

$$P(k) = C \exp(-\lambda k), \quad [2]$$

where the normalization constant C is

$$C = [1 - \exp(-\lambda)] \exp(\lambda k_{min}). \quad [3]$$

λ is the inverse scale parameter, and k_{min} is the lower limit on the exponential scaling. For $k_{min} = 1$ (as in our case), the discrete exponential distribution is equivalent to a geometric distribution where the geometric “success probability” parameter $p = 1 - \exp(-\lambda)$. The λ parameter was fit via a numerical optimization of maximum likelihood, and the exponential distribution was found to perform better than a discrete power law distribution ($P < 0.0005$ for each SCN, likelihood-ratio test) (45, 46). There was strong agreement between λ values for biologically distinct samples, indicative of common synchronization patterns across SCNs. Fig. S5 C and F demonstrates that the exponential distribution of node degree is consistent across thresholds, with changes in λ . Thus, we identified a consistent small-world discrete exponential functional network arising from SCN resynchronization.

Coupling Is Strongest in and Between Core SCN Regions. Commonly, studies of the SCN have revealed two clusters of cells: a ventral core region defined by excitatory (phase attractive) GABAergic connections, VIP production, and light input from the retinohypothalamic tract, and a dorsal shell region lacking these properties (16–19). To examine how this core-shell paradigm relates to the functional network, we examined the spatial hierarchy of the network. Fig. 5A illustrates the spatial hierarchy of node degree distribution across a representative SCN. A lower node degree was observed in the shell region, relative to the higher node degree generally seen in the SCN core, obtained by our inference method. We note that in each SCN, a number (average 45%) of cells in the SCN displayed no functional

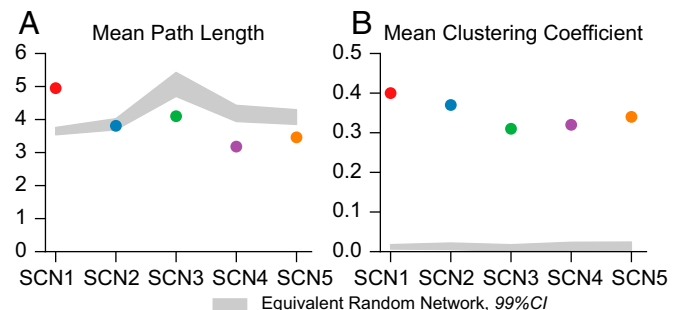


Fig. 3. SCN functional networks display small-world structure. (A) Average path length is on the same order of magnitude of an equivalent random (Erdos–Renyi) network. (B) Clustering coefficient is a magnitude greater than that of equivalent randomly generated networks. CIs are determined by generation of 10,000 equivalent Erdos–Renyi networks for each SCN.

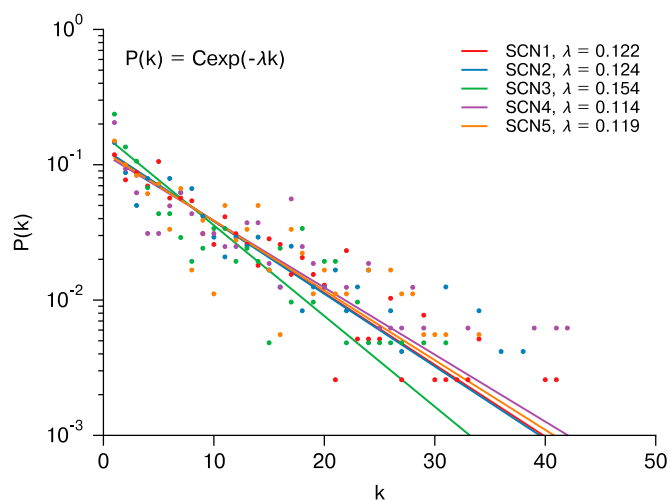


Fig. 4. Node degree (k) distributions for SCNs 1–5 plotted on a semilog scale. The resulting discrete exponential distributions $P(k) = C \exp(-\lambda k)$ were fit via numerical optimization of the maximum likelihood, resulting in distribution parameters λ for each network. Each SCN is better fit by a discrete exponential distribution than a discrete power law distribution (likelihood-ratio test, $P < 0.0005$ for each SCN). The strong agreement between λ shows a consistent network structure across SCNs. This agreement exists for a range of node degrees (Fig. S5).

connections. These cells are primarily located in the shell regions (Fig. 5A). This lack of functional connections does not indicate that there are no physiological connections, because shell neurons do resynchronize with the rest of the SCN. More likely, connections in this region are weaker and insufficient to rapidly resynchronize these cells above our functional connection MIC threshold. This structure is consistent even when accounting for phase lags between individual cells within the fully synchronized SCN (Fig. S4). Strikingly, this result of one cluster and the absence of a second cluster differs from prior studies of the functional organization of the SCN, which identified two phase clusters of neurons (19).

The distribution of functional path distances (d) is shown in Fig. 5B. The functional path distance is defined as the physical separation between two functionally connected cells. This distribution also appears exponential for each network, where the likelihood of a connection existing at distance d exponentially decays with this d . These distributions are not strictly unimodal; rather, SCNs 1, 2, 4, and 5 display a second peak (identifiable via continuous wavelet transform peak detection) that corresponds to the physical separation between core regions. SCN3 lacks this second peak as the identified cores of each half lack spatial separation. The presence of this second peak indicates that core-core functional connections within a SCN are more prominent than average long-range functional connections. Furthermore, it indicates that core-core coupling is tighter than core-shell coupling.

Relationship Between Physical and Functional Networks via Network Resimulation. Because the physical connections between cells cannot be directly probed, we focused on obtaining the functional network structure. Here, we simulated the TTX experiment using stochastic circadian oscillator networks (using models from refs. 33–35, detailed in Tables S1–S4) to determine how the functional network we infer is related to the underlying physical connectivity in the SCN. First, we tested the efficacy of this method for inferring simulated physical networks of 400 cells with either linear nearest neighbor, small world Watts–Strogatz (43), or random network topology. Next, we simulated the networks we inferred from SCN slices and show that our method can reinfer these physical networks with good accuracy. Details regarding these simulations are included in *SI Text*.

In Fig. S7, we show representative traces from these simulations and further demonstrate that our method is able to recapture the underlying physical networks (random, Watts–Strogatz small-world, nearest neighbor) with accuracy dependent on the density of connections. Functional networks inferred via our resynchronization and MIC method do not accurately recapture physical networks with dense random structure, as secondary indirect connections between nodes may be functionally identified as direct connections. To validate the consistency of specific network structures inferred from TTX experiments, we simulated the SCN networks discovered in the previous section and again inferred the network from these simulations. The resynchronization-MIC method performed well in recapturing simulated SCN networks, with an average area under the ROC curve (AUC) of 0.94 for the 3-state model and 0.80 for the more complex 11-state model. The ROC curves are plotted for each SCN in Fig. S8. We note that the false positives are most often incurred in distinguishing between primary and secondary connections within dense regions, whereas disconnected nodes are easily identified. Thus, this methodology can distinguish well between regions with dense and sparse physical connections such as the core and shell, but is less apt at identifying the individual physical connections in each region.

Discussion

In this work, we inferred the functional network of the suprachiasmatic nucleus during resynchronization through the use of a TTX-mediated resynchronization and the MIC. The functional networks we found were consistent across all samples, displaying small-world characteristics, a discrete exponential node degree distribution, and core-shell spatial hierarchy in which densely functionally connected cores synchronize rapidly. Our results are consistent with previous studies that show differences in function and neurotransmitter activity between core and shell SCN neurons (16–19, 25, 26, 47–49). However, in this work, for the first time to our knowledge, we probe connectivity within these clusters. This increased resolution leads to two surprising results: a lack of a second functionally connected cluster in the shell region and dense connections between SCN cores.

It is well established that exposure to artificial long day or light:dark:light:dark frequency doubling conditions can split the SCN into core and shell phase clusters, which oscillate with a large phase lag and also result in behavioral splitting (19, 48, 49). Although shell neurons form a phase cluster under these conditions, we found few functional connections within this region even when accounting for phase alignment, suggesting that the phase clustering is driven by a common response to light reception and mediated by the core SCN rather than driven by tight connectivity within the

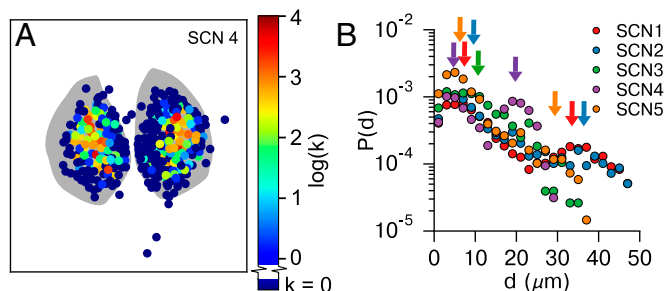


Fig. 5. Hubs of the small-world network are located in the central SCN. (A) Heatmap of node degree [color $\propto \log(k)$] distribution for a representative SCN shows that hubs of the small-world network are preferentially located in SCN core regions. All SCNs are shown in Fig. S6. (B) Connection length (d μm) distributions for SCNs 1–5 plotted on a semilog scale. Two peaks (arrows) are identifiable for SCNs 1, 2, 4, and 5: a local peak corresponding to connections between physically nearby neurons, and a second peak corresponding to the distance for functional connections between central SCN regions. For SCN3, these peaks are indistinguishable due to lack of spatial separation between cores.

shell itself. One particular advantage of the TTX assay we use is that light-based approaches are unable to differentiate between cells that have identical responses to a common stimulus and cells that communicate to establish similar behavior. A previous study of SCN reentrainment to shifted light exposure also showed that the ventral SCN reentrained rapidly, whereas the dorsal region took several days to reentrain (17). It was proposed that the core entrained rapidly due to its receiving input from the retinohypothalamic tract (RHT) and that synchronization of the shell was mediated by the effect of excitatory GABA. As our resynchronization conditions are chemically-induced and do not involve light input, it was unexpected that a fast-resynchronizing core/slow-resynchronizing shell is a conserved feature between these studies. This consistency indicates that the underlying structure of the SCN, rather than simply RHT connection, drives the dominant role of the core SCN.

We did not attempt to identify connection directionality or the molecular mechanisms driving connectivity, and it is possible that multiple pathways are involved. It has been shown that excitatory GABA action drives reentrainment of the shell region in response to light phase shifts (17). GABA action was examined in depth in recent collaborative works (16, 26); these studies demonstrated the encoding of day length through the GABA pathway, by the Cl^- -dependent excitatory (core, phase-attractive) or inhibitory (shell, phase-repulsive) effects of slow-scale (tonic) GABA. Visually, the core regions identified in our networks overlap with the regions of excitatory GABA action (26). In future studies, our TTX-based assay could be combined with VIP/GABA/glutamate agonist or antagonist application and repeated to identify the molecular mechanisms responsible for the identified connections. If GABA coupling affects differentiation between core hub neurons and shell neurons, this would result in significant seasonal plasticity of the functional network.

The functional networks we inferred contained a surprising number of connections between core regions of each suprachiasmatic nucleus. The SCN is often thought to be most tightly connected within each half, given the ability of the left and right SCN to oscillate in antiphase in animals exposed to constant light (50, 51). However, tight bilateral coupling is reflective of previous studies that showed significant coupling between the halves and further implicates the glutamate receptor in this communication (52). This possible involvement of the glutamate receptor is especially interesting, because the glutamate receptor has also been implicated in communication between the SCN and the RHT, which occurs in the core SCN region (53). Thus, our results support the hypothesis that antiphase oscillation between SCN halves in constant light is made possible by distinct signaling mechanisms in the SCN rather than a weaker coupling strength between halves (52, 54).

Theoretical studies in network science, as well as modeling studies specific to the circadian field, have pointed to possible advantages and causes of a small-world network structure. Small-world exponential networks provide advantages in robustness due to having hubs of high node degree and many less-important nodes of low node degree. Networks with this topology are better able to maintain short paths of communication when randomly selected nodes are removed (55), due to the redundancy and long-range connections provided by network hubs. Small-world topology has also been shown to enhance synchronization and amplitude properties of the SCN with a lower energy cost (fewer connections) compared with random and nearest-neighbor networks (21, 56). Theoretical studies have predicted that spatially embedded small-world networks, such as neuronal networks, would display an exponential node degree distribution as seen in our data (57, 58). This distribution would result from growth of a small initial population of connected nodes. As more nodes are added, the neuron population is forced to move spatially and initial local connections ultimately become long range while new short-range connections form. In this context, it is striking to note that the fetal SCN forms as neurons are added to the core first and then shell regions. The connections we measure, therefore, may reflect the ontogeny of synapse formation in the SCN. If, however, core-core long range connections are found to

be diffusive rather than synaptic, this hypothesis would not apply. Future experiments could test whether the left and right SCN must form synapses to synchronize, for example, in cocultures.

Our work presents both a perspective on connectivity within the SCN and a new assay for observing communication between individual circadian neurons at high spatial resolution. A major difficulty in mapping the SCN and the brain as a whole lies partly in the multiple time and physical scales at play. One method alone is insufficient to map the whole SCN at all resolutions, necessitating multiple perspectives to achieve spatial, directional, and mechanistic specificity. In conjunction with light-driven desynchronization assays, antagonist/agonist application, genetic knockdowns, and mathematical modeling, this TTX assay with correlation metrics can be used to further probe connections within the SCN at a single-cell level and between the SCN and other brain regions.

Materials and Methods

Cell Culture and Bioluminescence Recording. SCNs were obtained from 7-d-old homozygous PER2::LUC mice (founders generously provided by J. Takahashi, University of Texas Southwestern, Dallas) housed under a 12-h:12-h light:dark schedule. All procedures were approved by the Washington University Animal Studies Committee and complied with National Institutes of Health guidelines. Bilateral SCN from 300- μ m coronal sections of hypothalamus were cultured on Millicell-CM membranes (Millipore) in 400 mL air-buffered DMEM with two full-volume exchanges every 7 d. After 14 d *in vitro*, the culture was transferred to the stage of an inverted microscope (Nikon TE2000 fitted with a 20 \times objective and 0.5 \times coupler for a 10 \times magnification) inside a dark incubator (In Vivo Scientific). We add 0.15 mM beetle luciferin (BioThema) to the medium and imaged bioluminescence at 36 °C with an ultrasensitive CCD camera (Andor Ixon; 1 \times 1 binning, 1-h exposures). Cultures were then treated with 2.5 μ M TTX (Sigma) as previously described (36). TTX remained in the medium for 6 d while imaging continued. We then performed three full-volume exchanges of fresh medium and resumed recording for 8–12 d to monitor resynchronization of PER2::LUC rhythms. Bright field images before and after each recording were used to focus and align the culture with prior images.

Software was developed to locate and track neuron bioluminescence intensities in each image time series. In each frame, the software identified potential neurons using a standard difference of Gaussians blob detector. The algorithm took the set of neuron locations in each image and attempted to find spatial correspondences between them in the image time series. The correspondences were found by taking each potential neuron location and looking at previous images to find neurons in a nearby radius. Because neurons could be undetectable for multiple frames (when bioluminescence is low), the search was extended back in time multiple frames with a slowly increasing search radius. If the algorithm was able to connect a series of potential neuron locations through enough images, then it was assumed the sequence of locations represented a real neuron and the time series intensity was extracted from the images. If the algorithm could not form a sufficiently long sequence of locations, the neuron was discarded as noise. Results from automated neuron tracking were comparable to results obtained using manual tracking of neurons with ImageJ software (National Institutes of Health).

Numerical Methods. The MIC is calculated by partitioning a scatter plot of two variables (X and Y ; here, these are bioluminescence recordings from two cells) into an n_x -by- n_y grid g that maximizes mutual information $I_g(X; Y) = \sum_{y \in Y} \sum_{x \in X} p(x, y) \log[p(x, y)/p(x)p(y)]$ normalized by the maximal mutual information, $\log_{\min}\{n_x, n_y\}$, in g . The optimal grid is selected as in ref. 30, by computing the normalized mutual information for a subset of all possible grids bounded in resolution by $n_x \times n_y < B$. Details regarding this partitioning algorithm appear in the supplement to ref. 30. As suggested in ref. 30, we used binning parameter $B = N^{0.6}$, where N is the number of data points in a time series. The MIC was calculated through the minepy package for Python (with interfaces to C++, R, MATLAB, and Octave) (59). The threshold for connectivity was selected based on receiver operating characteristic curves. Data analysis and processing were performed using Python. Network properties were calculated using the Networkx package (60). Statistical tests for exponential and power law model fits were performed with the Python module powerlaw (46), in a manner according to ref. 45. Briefly, numerical optimization (rather than a continuous approximation) was used to fit discrete exponential and power law (ζ) models, and a likelihood-ratio test was applied to determine goodness-of-fit.

Stochastic Simulation. Stochastic simulation of circadian models was performed in Python with the StochKit2 implementation of the Gillespie algorithm in the GillesPy (<https://github.com/gillespy>) library (61).

ACKNOWLEDGMENTS. We thank Kelsey R. Dean, Brian Drawert, and Stephanie R. Taylor for helpful discussions. We also thank each of the anonymous reviewers, whose efforts have improved and shaped our manuscript. This

work was supported by NIH Grant 1R01GM096873-01 (to F.J.D., L.R.P., and E.D.H.) and Institute for Collaborative Biotechnologies Grant W911NF-09-0001 from the US Army Research Office.

- Refinetti R, Menaker M (1992) The circadian rhythm of body temperature. *Physiol Behav* 51(3):613–637.
- Nagoshi E, et al. (2004) Circadian gene expression in individual fibroblasts: Cell-autonomous and self-sustained oscillators pass time to daughter cells. *Cell* 119(5):693–705.
- Bieler J, et al. (2014) Robust synchronization of coupled circadian and cell cycle oscillators in single mammalian cells. *Mol Syst Biol* 10:739.
- Sassone-Corsi P (1998) Molecular clocks: Mastering time by gene regulation. *Nature* 392(6679):871–874.
- Bass J, Takahashi JS (2010) Circadian integration of metabolism and energetics. *Science* 330(6009):1349–1354.
- Lamia KA, Storch KF, Weitz CJ (2008) Physiological significance of a peripheral tissue circadian clock. *Proc Natl Acad Sci USA* 105(39):15172–15177.
- Kornmann B, Schaad O, Bujard H, Takahashi JS, Schibler U (2007) System-driven and oscillator-dependent circadian transcription in mice with a conditionally active liver clock. *PLoS Biol* 5(2):e34.
- Welsh DK, Logothetis DE, Meister M, Reppert SM (1995) Individual neurons dissociated from rat suprachiasmatic nucleus express independently phased circadian firing rhythms. *Neuron* 14(4):697–706.
- Liu C, Weaver DR, Strogatz SH, Reppert SM (1997) Cellular construction of a circadian clock: Period determination in the suprachiasmatic nuclei. *Cell* 91(6):855–860.
- Aton SJ, Colwell CS, Harmar AJ, Waschek J, Herzog ED (2005) Vasoactive intestinal polypeptide mediates circadian rhythmicity and synchrony in mammalian clock neurons. *Nat Neurosci* 8(4):476–483.
- Liu AC, et al. (2007) Intercellular coupling confers robustness against mutations in the SCN circadian clock network. *Cell* 129(3):605–616.
- Ananthasubramanian B, Herzog ED, Herzog H (2014) Timing of neuropeptide coupling determines synchrony and entrainment in the mammalian circadian clock. *PLoS Comput Biol* 10(4):e1003565.
- Ko CH, et al. (2010) Emergence of noise-induced oscillations in the central circadian pacemaker. *PLoS Biol* 8(10):e1000513.
- Vasalou C, Herzog ED, Henson MA (2011) Multicellular model for intercellular synchronization in circadian neural networks. *Biophys J* 101(1):12–20.
- An S, et al. (2013) A neuropeptide speeds circadian entrainment by reducing intercellular synchrony. *Proc Natl Acad Sci USA* 110(46):E4355–E4361.
- DeWoskin D, et al. (2015) Distinct roles for GABA across multiple timescales in mammalian circadian timekeeping. *Proc Natl Acad Sci USA* 112(29):E3911–E3919.
- Albus H, Vansteensel MJ, Michel S, Block GD, Meijer JH (2005) A GABAergic mechanism is necessary for coupling dissociable ventral and dorsal regional oscillators within the circadian clock. *Curr Biol* 15(10):886–893.
- Welsh DK, Takahashi JS, Kay SA (2010) Suprachiasmatic nucleus: Cell autonomy and network properties. *Annu Rev Physiol* 72:551–577.
- Evans JA, Leise TL, Castanon-Cervantes O, Davidson AJ (2013) Dynamic interactions mediated by nonredundant signaling mechanisms couple circadian clock neurons. *Neuron* 80(4):973–983.
- To TL, Henson MA, Herzog ED, Doyle FJ, 3rd (2007) A molecular model for intercellular synchronization in the mammalian circadian clock. *Biophys J* 92(11):3792–3803.
- Vasalou C, Herzog ED, Henson MA (2009) Small-world network models of intercellular coupling predict enhanced synchronization in the suprachiasmatic nucleus. *J Biol Rhythms* 24(3):243–254.
- Bernard S, Gonze D, Cajavec B, Herzog H, Kramer A (2007) Synchronization-induced rhythmicity of circadian oscillators in the suprachiasmatic nucleus. *PLoS Comput Biol* 3(4):e68.
- DeWoskin D, Geng W, Stinchcombe AR, Forger DB (2014) It is not the parts, but how they interact that determines the behaviour of circadian rhythms across scales and organisms. *Interface Focus* 4(3):20130076.
- Meijer JH, Michel S, Vanderleest HT, Rohling JHT (2010) Daily and seasonal adaptation of the circadian clock requires plasticity of the SCN neuronal network. *Eur J Neurosci* 32(12):2143–2151.
- Evans JA, et al. (2015) Shell neurons of the master circadian clock coordinate the phase of tissue clocks throughout the brain and body. *BMC Biol* 13:43.
- Myung J, et al. (2015) GABA-mediated repulsive coupling between circadian clock neurons in the SCN encodes seasonal time. *Proc Natl Acad Sci USA* 112(29):E3920–E3929.
- Freeman GM, Jr, Krock RM, Aton SJ, Thaben P, Herzog ED (2013) GABA networks destabilize genetic oscillations in the circadian pacemaker. *Neuron* 78(5):799–806.
- Yamaguchi S, et al. (2003) Synchronization of cellular clocks in the suprachiasmatic nucleus. *Science* 302(5649):1408–1412.
- Schwartz WJ, Gross RA, Morton MT (1987) The suprachiasmatic nuclei contain a tetradotoxin-resistant circadian pacemaker. *Proc Natl Acad Sci USA* 84(6):1694–1698.
- Reshef DN, et al. (2011) Detecting novel associations in large data sets. *Science* 334(6062):1518–1524.
- Egúiluz VM, Chialvo DR, Cecchi GA, Baliki M, Apkarian AV (2005) Scale-free brain functional networks. *Phys Rev Lett* 94(1):018102.
- Herzog ED, Aton SJ, Numano R, Sakaki Y, Tei H (2004) Temporal precision in the mammalian circadian system: A reliable clock from less reliable neurons. *J Biol Rhythms* 19(1):35–46.
- Gonze D, Goldbeter A (2006) Circadian rhythms and molecular noise. *Chaos* 16(2):026110.
- Schroder S, Herzog ED, Kiss IZ (2012) Transcription-based oscillator model for light-induced splitting as antiphase circadian gene expression in the suprachiasmatic nuclei. *J Biol Rhythms* 27(1):79–90.
- Abel JH, Widmer LA, St. John PC, Stelling J, Doyle FJ, III (2015) A coupled stochastic model explains differences in cry knockout behavior. *IEEE Life Sci Lett* 1(1):3–6.
- Webb AB, Angelo N, Huettnner JE, Herzog ED (2009) Intrinsic, nondeterministic circadian rhythm generation in identified mammalian neurons. *Proc Natl Acad Sci USA* 106(38):16493–16498.
- Buhr ED, Yoo SH, Takahashi JS (2010) Temperature as a universal resetting cue for mammalian circadian oscillators. *Science* 330(6002):379–385.
- Garofalo M, Nieuw T, Massobrio P, Martinoia S (2009) Evaluation of the performance of information theory-based methods and cross-correlation to estimate the functional connectivity in cortical networks. *PLoS One* 4(8):e6482.
- Bettencourt LM, Stephens GJ, Ham MI, Gross GW (2007) Functional structure of cortical neuronal networks grown in vitro. *Phys Rev E Stat Nonlin Soft Matter Phys* 75(2 Pt 1):021915.
- Kamiński M, Ding M, Truccolo WA, Bressler SL (2001) Evaluating causal relations in neural systems: Granger causality, directed transfer function and statistical assessment of significance. *Biol Cybern* 85(2):145–157.
- Pourzanjani A, Herzog ED, Petzold LR (2015) On the Inference of Functional Circadian Networks Using Granger Causality. *PLoS One* 10(9):e0137540.
- Fujita KA, et al. (2010) Decoupling of receptor and downstream signals in the Akt pathway by its low-pass filter characteristics. *Sci Signal* 3(132):ra56.
- Watts DJ, Strogatz SH (1998) Collective dynamics of ‘small-world’ networks. *Nature* 393(6684):440–442.
- Newman ME, Moore C, Watts DJ (2000) Mean-field solution of the small-world network model. *Phys Rev Lett* 84(14):3201–3204.
- Clauset A, Shalizi CR, Newman MEJ (2009) Power-law distributions in empirical data. *SIAM Rev* 51(4):661–703.
- Alstott J, Bullmore E, Plenz D (2014) Powerlaw: A Python package for analysis of heavy-tailed distributions. *PLoS One* 9(1):e85777.
- Yan L, Foley NC, Bobula JM, Kriegsfeld LJ, Silver R (2005) Two antiphase oscillations occur in each suprachiasmatic nucleus of behaviorally split hamsters. *J Neurosci* 25(39):9017–9026.
- Evans JA, Elliott JA, Gorman MR (2011) Dim nighttime illumination interacts with parametric effects of bright light to increase the stability of circadian rhythm bifurcation in hamsters. *Chronobiol Int* 28(6):488–496.
- Watanabe T, et al. (2007) Bimodal clock gene expression in mouse suprachiasmatic nucleus and peripheral tissues under a 7-hour light and 5-hour dark schedule. *J Biol Rhythms* 22(1):58–68.
- de la Iglesia HO, Meyer J, Carpino A, Jr, Schwartz WJ (2000) Antiphase oscillation of the left and right suprachiasmatic nuclei. *Science* 290(5492):799–801.
- Ohta H, Yamazaki S, McMahon DG (2005) Constant light desynchronizes mammalian clock neurons. *Nat Neurosci* 8(3):267–269.
- Michel S, et al. (2013) Mechanism of bilateral communication in the suprachiasmatic nucleus. *Eur J Neurosci* 37(6):964–971.
- Ebling FJ (1996) The role of glutamate in the photic regulation of the suprachiasmatic nucleus. *Prog Neurobiol* 50(2-3):109–132.
- Indic P, Schwartz WJ, Paydarfar D (2008) Design principles for phase-splitting behaviour of coupled cellular oscillators: Clues from hamsters with ‘split’ circadian rhythms. *J R Soc Interface* 5(25):873–883.
- Albert R, Barabási AL (2002) Statistical mechanics of complex networks. *Rev Mod Phys* 74(1):47–97.
- Hafner M, Koeppel H, Gonze D (2012) Effect of network architecture on synchronization and entrainment properties of the circadian oscillations in the suprachiasmatic nucleus. *PLoS Comput Biol* 8(3):e1002419.
- Ozik J, Hunt BR, Ott E (2004) Growing networks with geographical attachment preference: Emergence of small worlds. *Phys Rev E Stat Nonlin Soft Matter Phys* 69(2 Pt 2):026108.
- Zitin A, et al. (2014) Spatially embedded growing small-world networks. *Sci Rep* 4:7047.
- Albanese D, et al. (2013) Minerva and minepy: A C engine for the MINE suite and its R, Python and MATLAB wrappers. *Bioinformatics* 29(3):407–408.
- Hagberg AA, Schult DA, Swart PJ (2008) Exploring network structure, dynamics, and function using NetworkX. *Proceedings of the 7th Python in Science Conference*, eds Varoquaux G, Vaught T, Millman J (SciPy 2008, Pasadena, CA), pp 11–15.
- Sanft KR, et al. (2011) StochKit2: Software for discrete stochastic simulation of biochemical systems with events. *Bioinformatics* 27(17):2457–2458.
- Rougemont J, Naef F (2007) Dynamical signatures of cellular fluctuations and oscillator stability in peripheral circadian clocks. *Mol Syst Biol* 3:93.
- St John PC, Taylor SR, Abel JH, Doyle FJ, 3rd (2014) Amplitude metrics for cellular circadian bioluminescence reporters. *Biophys J* 107(11):2712–2722.
- St John PC, Doyle FJ, 3rd (2015) Quantifying stochastic noise in cultured circadian reporter cells. *PLoS Comput Biol* 11(11):e1004451.